Journal of Materials Science: Materials in Electronics (2018) 29:8523–8534
https://doi.org/10.1007/s10854-018-8866-x

ZnS@carbonaceous aerogel composites fabricated in production of hydrogen and for removal of organic pollutants

Junwei Lu[1] · Huihui Hu[1] · Saisai Yang[1] · Paramasivam Shanmugam[1] · Wei Wei[2] · Manickam Selvaraj[1] · Jimin Xie[1]

Received: 31 January 2018 / Accepted: 7 March 2018 / Published online: 14 March 2018

Abstract
Novel hollow sphere morphologied zinc sulphide@carbonaceous aerogel (ZnS@CA) composites with different ZnS content were fabricated using a simple hydrothermal carbonization treatment following by a facile in situ growth method. The fabricated composites were used as catalysts for chemical degradation of the methylene blue (MB) and for hydrogen evolution. Our photocatalytic studies are found, from the photocatalytic results obtained by different ZnS@CA materials, that 55 wt%ZnS@CA exhibits the excellent photocatalytic performances for MB degradation and the highest rate of hydrogen production that are correspondingly 1.7- and 8.1-fold higher than that of pure ZnS. This improved photocatalytic performance could be mainly attributed by unique 3D catenulate carbon networks, which can be highly favorable to disperse of ZnS on the surface of CA. An synergetic properties between CA and ZnS could be highly beneficial to the photo-generated electron–hole separation. The hollow microsphere structured ZnS nanoparticles allow multi-reflections of light within the interior cavity and increases the capture efficiency of visible light. A possible photocatalytic mechanism of the main active radicals has also been proposed. This work opens up the new prospects for a low-cost biomass-based sulfide photocatalysts used for the environmental purification and hydrogen generation.

1 Introduction

In the recent years, the environmental problems and global energy crisis have become the most pivotal issues, which are important to our lives. In both these areas, utilization of solar power as an energy source through the employment of heterogeneous photocatalytic processes has become one of the most effective strategies for the remediation of polluted water and the production of clean energy [1–3]. The various materials such as oxides [4], sulfides [5], oxynitrides [6], and organic metal complexes [7] have been reported to obtain highly efficient photocatalysts. Among them, the different types of nanostructured metal sulfides like Ag_2S, NiS, ZnS, PbS, and Sb_2S_3 have been also developed because of their potential applications in environmental sectors, optical, electronic and energy [8–10]. Among these sulfide semiconductor photocatalysts, ZnS photocatalysts have been recognized as promising photocatalysts, because of their low toxicity, easy preparation, strong oxidation and high conduction band (CB) (−0.9 eV) [11]. Unfortunately, a few drawbacks still exist in the single component system including well-known photocorrosion, the low efficiency of charge separation and facile particulate aggregation [12]. Therefore, the researchers had been expended with their efforts to find a promising method for suppressing the recombination rate of electron–hole pairs during photocatalytic activity of ZnS under visible-light irradiation. Many literature reports describe to improve the photocatalytic activity by the conventional photocatalytic materials which can rush an efficient separation of electron–hole pairs, such as semiconductors [13], graphene [14], precious metals [15, 16] and carbon nanotubes [17]. For instance, Patil et al. synthesized the effective ZnS–graphene nanocomposites using a microwave irradiation method [18]. Gu et al. have also synthesized carbon nanotube/ZnS heterostructures by a solution chemical

Electronic supplementary material The online version of this article (https://doi.org/10.1007/s10854-018-8866-x) contains supplementary material, which is available to authorized users.

✉ Manickam Selvaraj
chems@ujs.edu.cn

✉ Jimin Xie
xiejm391@sohu.com

[1] School of Chemistry & Chemical Engineering, Jiangsu University, Zhenjiang 212013, People's Republic of China

[2] Center of Analysis and Test, Jiangsu University, Zhenjiang 212013, People's Republic of China

method [19]. Hsu et al. synthesized the three-dimensional ZnO@ZnS–Ag_2S core–shell nanorods heterostructures using a hydrothermal method [20]. However, the preparation methods mentioned above mostly have many limitations, such as expensive process, time-consuming, toxic, tedious steps, compared to the preparation of carbonaceous aerogels (CA).

Three-dimensional (3D) biomass-derived CAs are quickly becoming the focus of the current research areas due to their high porosities (80–98%), high surface areas (400–1100 $cm^2\ g^{-1}$), low densities and low electrical resistivities (≤ 40 mΩ cm), which make them as an ideal candidates for heterogeneous catalysts [21, 22]. Due to these special chemical and textural characteristics, the CA materials possesses the promising applications of adsorbents, photocatalysts and supercapacitors. For instance, Li et al. have successfully prepared the three-dimensional carbon aerogels for adsorbent organic solvents and oils [23]. Ren et al. have fabricated the MnO_2@CA nanocomposites to use as an electrode material [24]. Miao et al. synthesized a BiOBr/CA composite, proved it as an outstanding adsorption material by the studies of photodegradation of organic pollutants under visible light irradiation [25] and demonstrated that CA is a capable substrate for the photocatalysts by virtue of the efficient initiation, a rapid photoinduced charged separation and the relatively slow charge recombination. This behavior is attributed to the qualities of the CA including large specific surface area with enhanced efficiency for the capture of visible light irradiation through multiple reflection of light [26]. At the same time, the CA exhibits the excellent synergetic properties for photodegradation activity. To the best of our knowledge, there is no report on the synthesis of ZnS@CA materials using fresh radishes. The full potential of this material in practical photocatalytic settings is highly desired to be realized.

Herein, for the first time, the ZnS@CA materials were synthesized using fresh radishes as an economical and ubiquitous biomass raw material. This process is a facile and totally green synthetic method, without any centrifugation, sonication and toxic reagent. Compared with the published chemical methods, this procedure is an effective method for large-scale production. Characteristic of the ZnS@CA composites and their catalytic performance were extensively investigated. The possible photocatalytic mechanism of obtained samples were also discussed in detail.

2 Experimental

2.1 Materials

Fresh radishes were purchased from local markets and fully washed with deionized water before use. All chemical reagents viz., thioacetamide (C_2H_5NS), Zinc nitrate hexahydrate [$Zn(NO_3)_2{\cdot}6H_2O$] and absolute ethanol (C_2H_6O) were used without further purification and purchased from Sinopharm Chemical Reagent Co., Ltd. Deionized water was completely used to our research works.

2.2 Catalyst preparation

2.2.1 Preparation of carbonaceous hydrogel (CAH)

To prepare the CAH, the fresh radishes were peeled, cut into square-sized ($2\times2\times3\ cm^3$) using a sharp knife, transferred to Teflon-sealed autoclave, which was heat-treated at 180 °C for 15 h. After cooling it to room temperature, for getting CAH, the as-obtained black CAH was washed by a mixture of water and ethanol (volume ratio: 1:1) for removal of soluble impurities. The corresponding carbonaceous aerogel (CA) was obtained by cutting the CAH into small pieces followed by lyophilizing treatment for 24 h using a high vacuum freeze-drying process at − 51 °C.

2.2.2 Synthesis of ZnS@CA

The ZnS@CA composites were synthesized using a facile fabrication method. In a typical synthesis procedure, 4.8 mmol of $Zn(NO_3)_2{\cdot}6H_2O$ was dissolved in 20 mL of deionized water, then 12 g of CAH was fully immersed in the mixture solution and shaken for 12 h. Thereafter, the resulting solution was immersed in hot water, and then thioacetamide (4.7 mmol, TAA) was added to it, and final mixture was kept at 70 °C for 6 h. After completing the reaction, the reaction was quenched through placing the mixture into an ice water bath. Then prepared sample was submerged in a mixture of water and ethanol (volume ratio: 1:1) for removal of impurities on the surface of ZnS@CAH. Finally, the ZnS@CA was obtained by lyophilizing of ZnS@CAH composite for 24 h using a high vacuum freeze-drying process at − 51 °C. The above similar method was used to synthesize other ZnS@CA composites, namely 25%ZnS@CA, 40%ZnS@CA, 55%ZnS@CA and 65%ZnS@CA, using 25, 40, 55 and 65 wt% of ZnS without changing of CAH, and also carried out for preparation of ZnS only.

2.3 Characterization

The structural information of the prepared samples were obtained using an X-ray diffractometer (Bruker AXS Company, Germany). FT-IR spectrum of the prepared samples was performed on a Nicolet FT-IR spectrophotometer (Nexus 470, Thermo Electron Corporation) using the KBr pellet method. Surface analysis of the sample was examined by X-ray photoelectron spectroscopy (XPS) using an ESCA PHI500 spectrometer. A scanning electron microscopy (SEM, JEOL-6701F) was used under a voltage

of 10 kV to examine the morphology of samples. The Brunauer–Emmett–Teller (BET) specific surface area of the samples was carried out by N_2 adsorption. Thermogravimetric analysis (TG) were obtained on SDTQ600 V5.0 Build 63 (TA instruments, USA) system in N_2 atmosphere at a heating rate of 10 K min^{-1}. UV–vis diffuse reflectance spectra (UV-DRS) were recorded by using Shimadzu UV-2450 spectrophotometer. Transmission electron microscopy (TEM) and high resolution-transmission electron microscopy (HRTEM) images were collected using a JEOL-JEM-2100 (JEOL, Japan) electron microscopy with an accelerating voltage of 200 kV. The fluorescence spectra of the samples were obtained by a QuantaMaster™40 spectrofluorimeter equipped with QuantaMaster & TimeMaster (Photon Technology International, USA).

2.4 Photocatalytic activity for degradation of MB

Photocatalytic activity of the samples were evaluated by the degradation reaction of MB (40 mg L^{-1}) under irradiation of a 500 W xenon lamp with a 420 nm cutoff filter. To determine the catalytic activity, 40 mg of 55 wt%ZnS@CA was suspended into 40 mL of the above MB solution. Before irradiation, the suspension was magnetically stirred for 30 min in the dark environment to reach adsorption–desorption equilibrium. During every irradiation interval, 4 mL of the suspension was withdrawn and centrifuged to remove the particles. The characteristic absorption peak of MB in the solution was determined using a UV-2450 spectrophotometer (around photo-absorption intensity at 664 nm). The similar experiments were done using the other ZnS@CA catalysts to find the optimum parameters along with a suitable photocatalyst.

2.5 Photocatalytic hydrogen production

The visible light-induced H_2 evolution tests were performed in a 100 mL 3-neck Pyrex flask connected to a closed gas cyclic system. Low power UV-LEDs (3 × 4 W, 420 nm) (Shenzhen LAMPLIC Science Co. Ltd, China), which were positioned 1 cm away from the reactor in four different directions and used as light sources to prompt the photocatalytic reaction. The illumination intensity at the catalyst surface is 60.0 mW. In a typical experimental procedure, 50 mg of 55 wt%ZnS@CA was dispersed in an aqueous solution (80 mL) containing 25 vol% methanol for hydrogen evolution determination. Prior to irradiation, the system was bubbled with nitrogen through the reactor for 40 min to assure anaerobic conditions. Furthermore, all the reactions were performed at 293 K under constant stirring. A portion (0.4 mL) of gas was intermittently sampled through a septum, and the hydrogen was analyzed by gas chromatography (GC-14C, Shimadzu, Japan, TCD, with nitrogen as a carrier gas and 5 Å molecular sieve column).

3 Results and discussion

3.1 Structural analysis (XRD)

The X-ray diffraction (XRD) patterns of the prepared samples such as CA, ZnS and ZnS@CA composites are shown in Fig. 1. Compared with JCPDS card no. 75-1621, the XRD pattern of CA exhibits a broad diffraction peak around at 23° which corresponds to diffraction from carbon (002) plane of graphite and suggested that the CA microsphere is an amorphous structure, as reported in elsewhere [27]. In literature, all the diffraction peaks can be well indexed to the cubic phase for pure ZnS [28]. For ZnS@CA samples, the main XRD diffraction peaks observed at 2θ values of 28.5°, 33.3°, 47.5°, 56.5°, 69.6° and 76.9° exhibit correspondingly to the crystal planes of (111), (200), (220), (311), (400) and (331) by (JCPDS, no. 05-0566) [29], suggested that the cubic natured ZnS nanoparticles are completely dispersed on the surface of CA. It is found that the broad peaks on ZnS@CA samples become into sharp peaks with higher intensities when the ZnS nanoparticles are increasing from 25 to 65% and to confirm that more cubic natured ZnS nanoparticles have been well-dispersed onto the surface of CA. Moreover, the above XRD patterns indicate that the incorporation into the CA does not change the phase structure of ZnS microspheres.

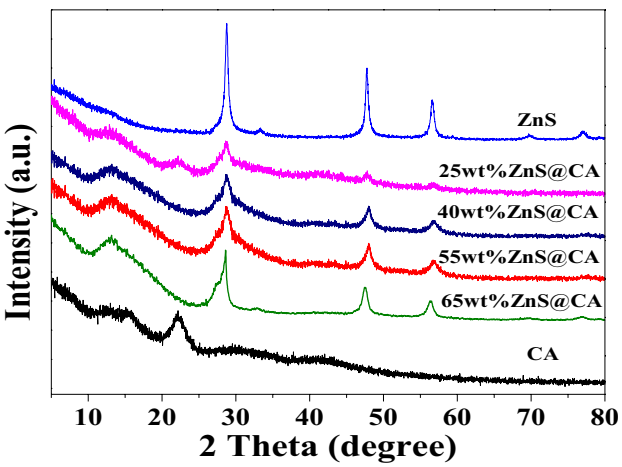

Fig. 1 The XRD patterns of CA and ZnS@CA synthesized with different ZnS content

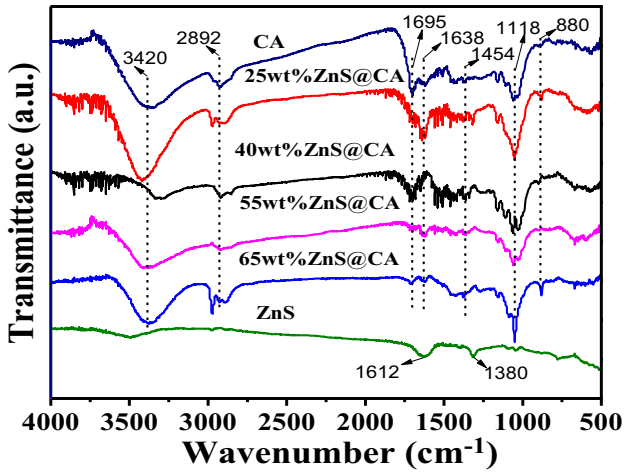

Fig. 2 FTIR spectra of CA and ZnS@CA synthesized with different ZnS content

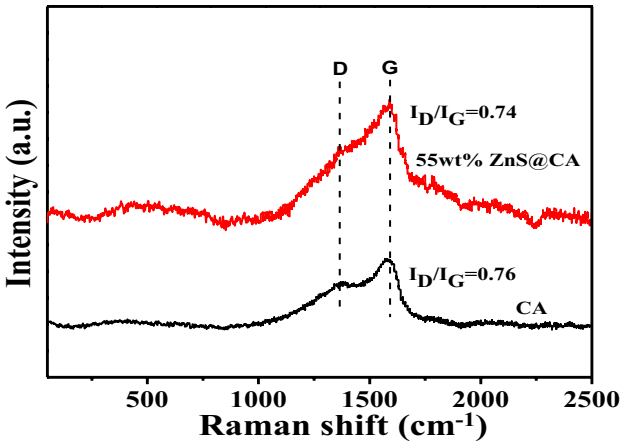

Fig. 3 Raman spectra of CA and 55 wt%ZnS@CA

3.2 Optical properties

To further observe the surface functional groups of ZnS@CA composites, FT-IR spectroscopy is measured and shown in Fig. 2. In the FT-IR spectrum of CA, the broad and strong band at 3420 cm^{-1} is contributed to O–H stretching vibrations. The observed bands at 1695 and 1638 cm^{-1} are correspondingly attributed to the C=O and C=C stretching vibrations, indicating that furanic and aromatic groups are highly presented in CA, as reported in literature [30]. The wavenumber at 1445 cm^{-1} can be attributed to either carboxylic O–H deformation vibration or C–H in-plane bending vibration, as reported in elsewhere [31]. The bands at 1118 is ascribed to the C–O–C stretching vibration or C–C framework vibration [32, 33]. The bands at 920 and 620 cm^{-1} are ascribed to deformation vibration of vinyl C–H and C–H plane bending vibration, respectively [34]. The FT-IR result indicates that the surfaces of CA have the rich amounts of hydroxyl, carbonyl, carboxyl, and aromatic groups. The surface groups provide the possibilities for their further functionalization and produce hydrophilic and hydrophobic nature on the surface of CA. The hydrophilic nature enhances to incorporate the ZnS nanoparticles on the surface of CA. The hydrophobic nature increases the stability of ZnS@CA. Moreover, the results of the FTIR analysis prove that the ZnS was successfully anchored to the CA.

The Raman spectrum is also applied in order to determine the interaction among ZnS and the CA. Raman spectra for CA and 55 wt%ZnS@CA are shown in Fig. 3 and describe that the broad and strong bands at about 1580 and 1358 cm^{-1} confirm the D and G band, respectively, those can be correspondingly attributed to the in-plane bond-stretching motion of the pairs of C-sp2 atoms and the disorder-induced mode associate with structure defects and imperfections [26]. The intensity values of D and G bands ratio (ID/IG) of 55 wt%ZnS@CA is lower than that of CA because the larger numbers of ZnS anchored on the surface of CA while this information proves to enhance their photocatalytic activity. In addition, the intensity values of D and G bands (ID/IG) of CA also strongly confirm the carbon raw materials are majorly converted into graphitized with a disordered structure.

3.3 XPS measurements

XPS analysis was performed on a typical 55 wt% ZnS@CA sample to verify the surface chemical state of elements. As shown in Fig. 4a, it is found that the product majorly contains C, Zn and S elements from the entire XPS spectrum. It is proposed that the peak of primary C 1s located at 284.5 eV could be assigned (Fig. 4b) to elemental carbon, which attributed to sp^2 hybridized C [26, 35, 36]. Another binding energies located at 285.9 and 287.1 eV imply that the different carbon groups are present on the surface of CA, which are correspondingly assigned to C=C–O, C–O/C=C groups [34, 36, 37]. The oxygen functional groups are somewhat available on the surface of CA because the trace amounts of raw materials could not be carbonized at 180 °C during the hydrothermal treatment process. As shown in Fig. 4c, the Zn 2p spectrum contains a doublet-feature at 1021.1 and 1044.2 eV, which refer to Zn $2p_{3/2}$ and $2p_{1/2}$ binding energies, respectively [38, 39]. In addition, the binding energy difference among the two lines is 23.1 eV, which confirms that Zn ions existed mainly with +2 oxidation state. The S 2p peak was fitted into two peaks which were assigned to sulfur anions in the lattice of ZnS (Fig. 4d). The peaks locate at 160.6 and 161.2 eV could be separately assigned to S $2p_{3/2}$ and S $2p_{1/2}$, respectively. Obviously, the above results from XPS, XRD and FT-IR confirm that the ZnS nanoparticles are majorly anchored on the surface of CA.

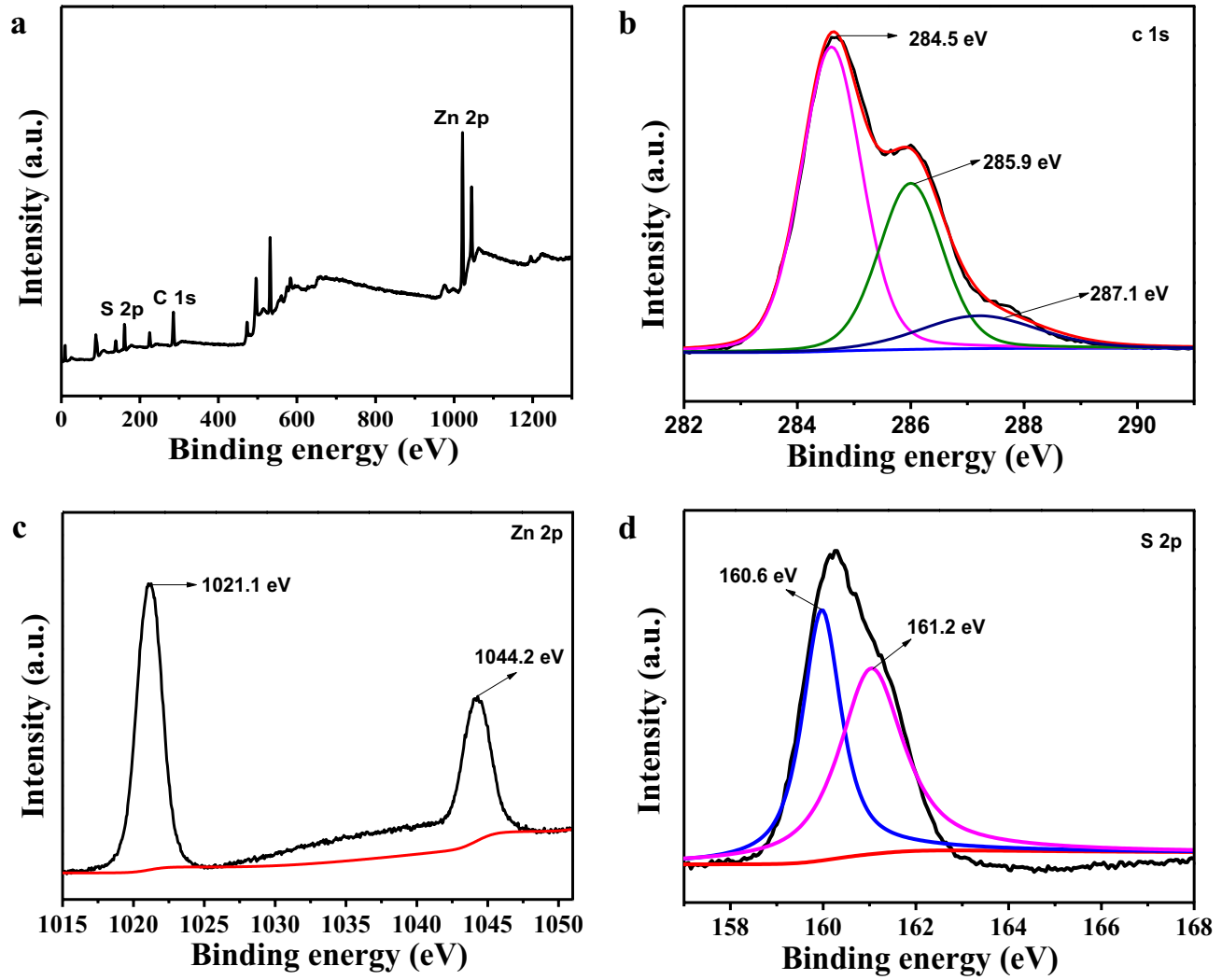

Fig. 4 XPS spectra of **a** 55 wt%ZnS@CA, **b** C 1s, **c** Zn 2p and **d** S 2p

3.4 SEM and TEM analysis

The morphology and structure of ZnS@CA photocatalysts were further investigated by TEM and SEM. As shown in Fig. 5a, the ZnS microspheres are uniformly distributed on the surface of CA which has 3D porous structure with a catenulate carbon networks that significantly preclude the agglomeration of the ZnS nanoparticles during the synthesis under hydrothermal method. A TEM image of the ZnS@CA material is shown in Fig. 5b, it is outward that the ZnS exists the hollow sphere morphology and are highly dispersed on the surface of the CA with a size of 100–150 nm (Fig. S1). It can be clearly seen that the ZnS and CA exhibit enhanced interface contact through the high magnification TEM image and shown in Fig. 5c. Typically, the difference in contrast between the pale center and the dark edge of the ZnS nanoparticles confirms the hollow nature structure. The hollow spherical structure of the ZnS nanoparticles is beneficial for light-scattering into the interior cavities, which can increase the capture efficiency of visible light and thereby generate more photogenerated electron–hole pairs [40]. A corresponding high-resolution TEM image of ZnS@CA is demonstrated in Fig. 5d and further certify the intimate interfacial contact between ZnS and CA. Notably, distinct lattice fringes could be directly observed from HRTEM image with an interlayer spacing of 0.270 and 0.312 nm, which matches well with (200) and (111) planes of ZnS on the surface of CA. It is worthy found that the synergetic properties and the enhanced interface contact (Fig. 5d, marked in the red dash line) between the ZnS and CA could enhance to increase the charge transfer for leading photocatalytic reaction. According to the SEM, TEM and HRTEM images, the CA with the unique 3D catenulate carbon networks structure is beneficial to uniformly distributed ZnS on the surface through a facile in situ growth method.

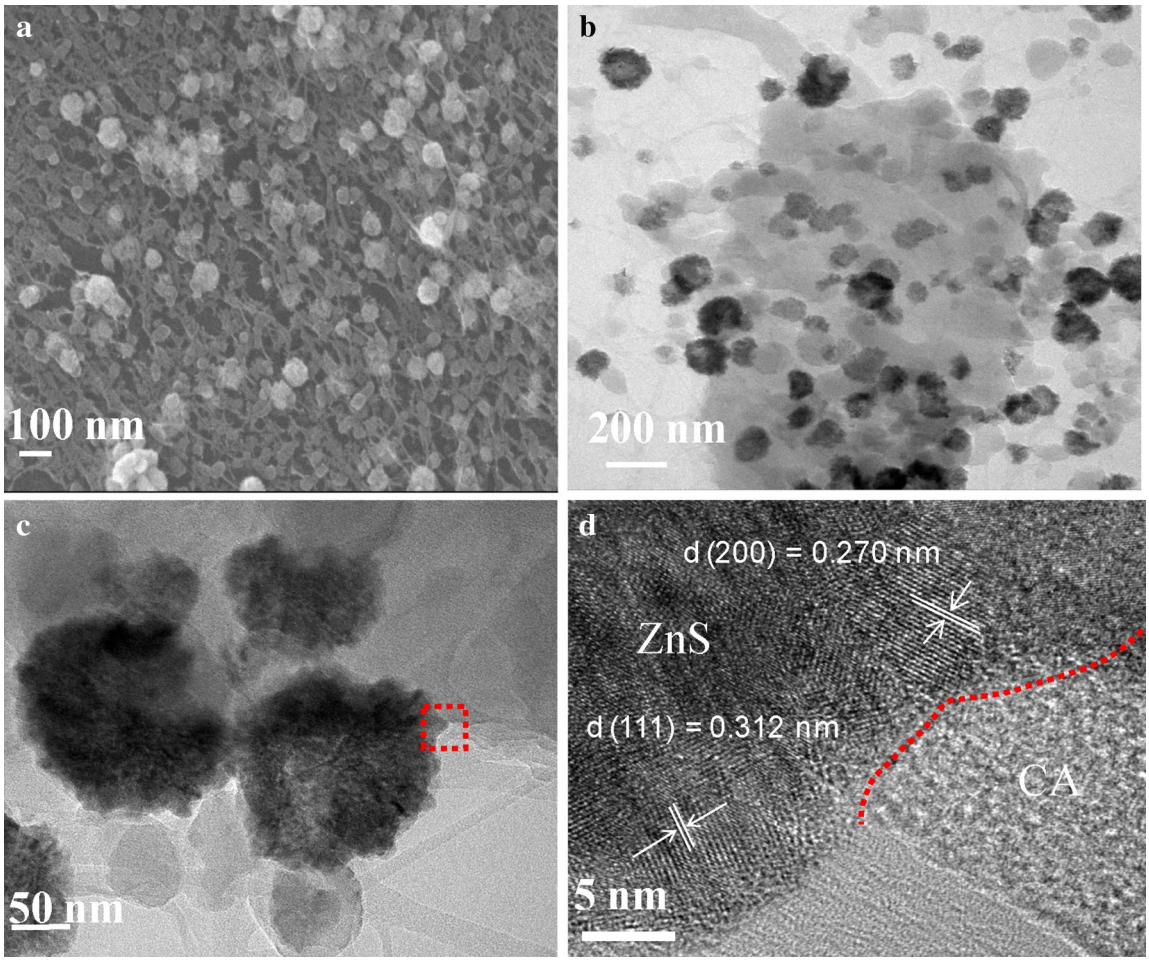

Fig. 5 **a** SEM image; **b** and **c** TEM images, and **d** HRTEM image of 55 wt%ZnS@CA

3.5 N_2-sorption and thermogravimetric studies

It is well-known that the large surface area of composite is beneficial for the enhancement of photocatalytic performance because of rich active sites on the surface, which enhances to improve catalytic activity and adsorption efficiency by photocatalytic chemisorption [41]. The BET surface area of 55 wt%ZnS@CA is higher as compared to that of CA because of higher loading of ZnS on the surface of CA and the N_2 adsorption–desorption isotherms is as shown in Fig. 6. The introduction of ZnS into the CA resulted in an increase in the surface area of the CA, which allowed for better adsorption of pollutants and greater contact time between the catalyst and the adsorbed pollutants, which would undoubtedly improve the rate of the photocatalytic reaction. An increase in the BET surface area is probability due to the CA with 3D porous network structure preclude the agglomeration of the ZnS nanoparticles. Thus, the large surface area would help to increase the photocatalytic reaction sites for the adsorption water and reactant molecules, which

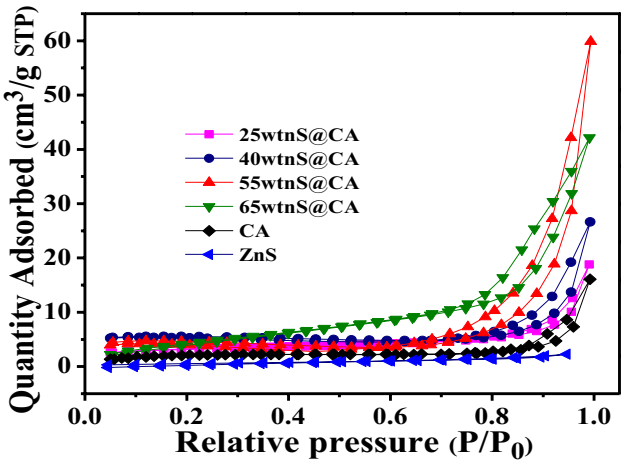

Fig. 6 N_2 isotherms of CA and ZnS@CA synthesized with different ZnS content

would lead to the enhancement of H_2 production and dye photodegradation. In order to reach the stability of CA, the thermogravimetric (TG) analysis of the CA was exhibited in Fig. S2. According to the TG curves, the thermal stability of 55 wt%ZnS@CA is better than the pure CA between 0 and 200 °C. Based on to the results for the initial thermal curves showing the thermally stable level, it appeared that the introduction of ZnS nanoparticles as a nanofiller in the CA may have improved thermal stability of the ZnS@CA composite over that of the pure CA [24].

3.6 UV–vis diffuse reflection spectra

The optical absorption property of semiconductor plays an important role in photocatalytic process. As shown in Fig. 7, the light absorption ability of prepared ZnS and ZnS@CA prepared with different ZnS content were characterized by UV–vis diffuse reflectance spectroscopy. It is quite apparent from these results that the optical absorption edge of pristine ZnS was around 365 nm and the band gap energy was found to be 3.42 eV. The optical absorption of ZnS@CA materials in the UV-light region was memorably enhanced and the absorption edges shifted to longer wavelengths when compared to pure ZnS. This CA modification to the ZnS narrows the material band gap, as well as the positive synergetic effects among the ZnS and CA components, may account for this enlarged absorption which would lead to the excellent photocatalytic activities [26, 42]. Furthermore, the CA with a 3D porous structure provide the sufficient contact interface with ZnS and a lot of spaces for the light enter in. After being combined with CA, the 55 wt%ZnS@CA exhibits the higher intense visible-light absorption, which could produce more efficiently utilization of solar irradiation which can be generated the rich electron–hole pairs.

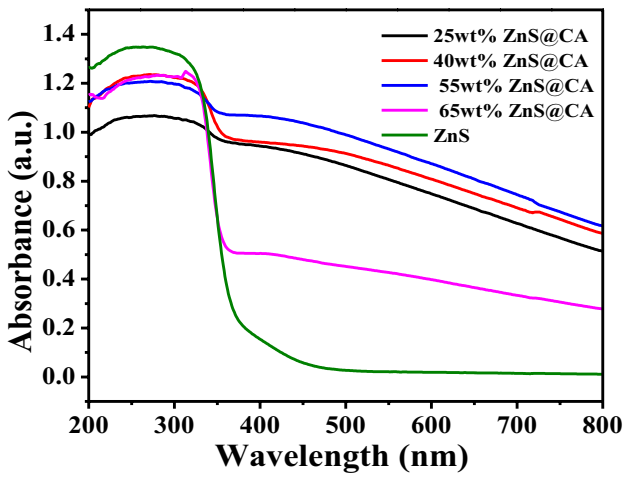

Fig. 7 UV–vis DRS of ZnS and ZnS@CA. (Color figure online)

3.7 Photocatalytic activity of ZnS@CA

3.7.1 Photocatalytic degradation of MB

The MB is one of the Industrial organic dyes and can be regarded as one of the pollutant sources in water. In this study, in order to ensure to increase the photocatalytic activity we chose high target pollutant concentration of 40 mg L^{-1}. The respective photocatalytic performances of ZnS, ZnS@CA materials were investigated by the photodegradaion of MB (40 mg L^{-1}) solution under visible-light irradiation. Firstly, an absorption–desorption balance has been achieved between the catalyst and MB solution after stirring 30 min without light irradiation. The color variation of MB in solution, changed from blue to light blue, and latterly disappeared under visible light illumination, indicating that MB dye was mostly degraded. In the absence of photocatalyst, the MB solution is hardly self-photolysis until the test period, demonstrating that MB is quite stable [43]. In the case of pure ZnS, the degradation ratios of MB only reached 50% under visible light irradiation for 180 min. As expected, the photocatalytic activity of all the ZnS@CA materials was higher than that of pure ZnS, which indicated that the CA had insignificant effect to improve the photocatalytic performances as compared to ZnS@CA materials. By contrast, the 55 wt%ZnS@CA shows the highest photocatalytic performances and produces the degradation of 91% of MB in 180 min as shown in Fig. 8a. This result can be highly attributed by increasing of BET surface area and synergistic reaction of the 55 wt%ZnS@CA material in the photodegradation reaction. In addition, the unique 3D porous network structure of 55 wt%ZnS@CA increases the efficiency of the capture of visible light through multi-reflection of the available light [44]. From the UV–vis absorption spectra, the 55 wt%ZnS@CA exhibits a high intensive light absorption in the visible light region, which generates more electron–hole pairs. We further investigate the kinetic behaviors of ZnS@CA for photodegradation of MB. The photocatalytic degradation kinetics of MB was exhibited in Fig. 8b. It can be observed that the reaction of MB photodegradation process confirms to pseudo-first order reaction kinetic model was used as follows (1),

$$\ln\left(C_0/C\right) = kt \tag{1}$$

where k is the apparent reaction rate constant, C_0 is the initial concentration of MB, C is the MB concentration at time t (mg L^{-1}). The greater k is, the faster reaction rate is. It can be found that the rate constants for all ZnS@CA materials are higher than pure ZnS. The k value of 55 wt%ZnS@CA can reach to 0.00967 min^{-1}, which was about 3.7 times of pure ZnS. That is to say, the 55 wt%ZnS@CA materials

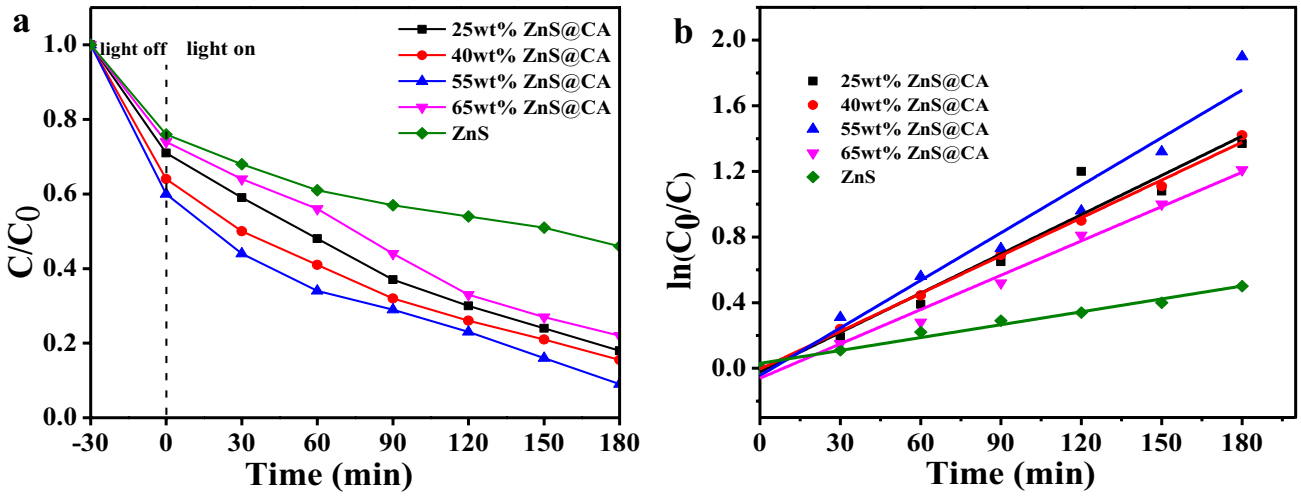

Fig. 8 **a** Visible light-induced photocatalytic degradation of MB. **b** Pseudo-first-order kinetics curves of MB degradation over different ZnS@CA catalysts

Table 1 Pseudo-first-order rate constant for photocatalytic oxidation of MB under different ZnS@CA catalysts

Photocatalyst	The first order kinetic equation	k (min^{-1})	R^2
ZnS	$\ln(C_0/C) = 0.00262\ t$	0.00262	0.99111
25 wt% ZnS@CA	$\ln(C_0/C) = 0.00798\ t$	0.00798	0.97343
40 wt% ZnS@CA	$\ln(C_0/C) = 0.00768\ t$	0.00768	0.99872
55 wt% ZnS@CA	$\ln(C_0/C) = 0.00967\ t$	0.00967	0.98159
65 wt%ZnS@CA	$\ln(C_0/C) = 0.00698\ t$	0.00698	0.99453

have greater photocatalytic performances than pure ZnS. As shown in Table 1, their rate constants (k), regression coefficients (R^2) and the kinetics equations for each photocatalyst are reported. Moreover, the 55 wt%ZnS@CA shows higher photocatalytic activity than other ZnS containing materials (see Table S1).

The stability of the 55 wt%ZnS@CA was also evaluated by recyclability for the degradation of MB under visible light irradiation. It is can be seen that the activity of the 55 wt%ZnS@CA decreases slightly after four test cycles (Fig. 9a), which indicates that the 55 wt%ZnS@CA is quite stable during the photocatalytic degradation of MB. This reveals that 55 wt%ZnS@CA displays a less photocorrosion during the photocatalytic oxidation of MB. In Fig. 9b, the XRD patterns of 55 wt%ZnS@CA and reused 55 wt%ZnS@CA are almost similar. The above results suggested that the synthesized catalysts have a high stability during the applications in organic dye removal.

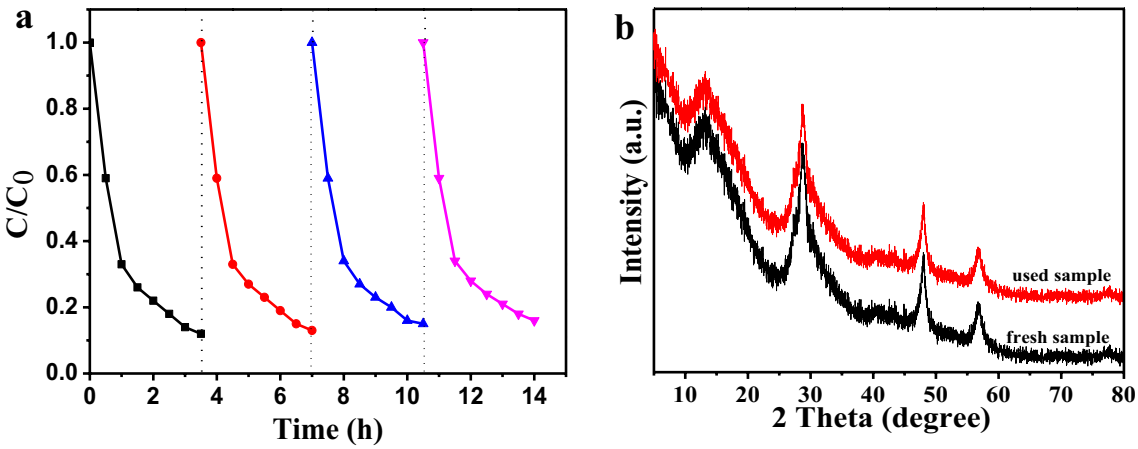

Fig. 9 **a** Stability tests of photocatalytic degradation of MB by 55 wt%ZnS@CA and **b** XRD patterns of the 55 wt%ZnS@CA before and after using of recycle reactions

3.7.2 Photocatalytic hydrogen production activity

Hydrogen is considering as a green energy source with excellent energy capacities and clean combustion products. To explore the performance of photocatalysts synthesized by us, the H_2 evolution experiments were further performed under visible-light irradiation. The experiments of hydrogen production were performed by taking 50 mg of the photocatalyst into 80 mL of a 25 vol% methanol solution. No appreciable hydrogen evolution was observed in the absence of either photocatalyst or irradiation, indicating that H_2 was produced from the actual photocatalytic experiment. Figure 10a shows the H_2 evolution plots of pure CA, ZnS and ZnS@CA materials. With pure CA and ZnS alone, no noticeable hydrogen evolution was detected. The above results demonstrated that pure ZnS and CA were inactive for photocatalytic H_2 evolution under the same conditions. But, the 55 wt%ZnS@CA shows a very high rate of hydrogen production. Because the introduction of ZnS into CA gives a strong effect on the rate of photocatalytic hydrogen evolution. A further comparison of the average hydrogen evolution rates of Zn@CA catalysts is presented in Fig. 10b. As shown, the rate of hydrogen production increases with increasing of ZnS loadings on the surface of CA up to 55 wt%, which corresponds to a rate of about 8.1 μmol h^{-1}. A further increase in the ZnS loading led to a reverse of this trend, which is attributed to the shielding of the incident light by the excess ZnS that covers the CA greatly suppressing the deformation of photogenerated carriers [45]. In addition, the photocatalytic activity of ZnS@CA in hydrogen production is higher than that of many previous reported about ZnS containing carbon photocatalysts, which were published as supporting information (Table S1). The photocatalytic H_2 production activity result is also similar to the photocatalytic degradation of MB results. The surface area, the degradation ratios of MB and the average hydrogen production rates of the catalysts were summarized in Table S2.

3.8 Possible photocatalytic mechanism

3.8.1 Photoluminescence spectra analysis

It is evident that photoluminescence (PL) spectra is applied to evaluate the separation efficiency of the photo-generated electron–hole pairs in a semiconductor, in which the higher PL intensity indicates a faster of recombination occurs [46, 47]. Figure 11 illustrates the PL spectra of ZnS@CA materials and pure ZnS with a maximum emission peak appeared at 425 nm with an excitation wavelength of 320 nm. Compared with ZnS, the CA and ZnS@CA materials are hardly altered about the spectral emission peak position, but the emission intensity of PL spectra significantly decreases. The results reveals that the ZnS@CA materials has a lower

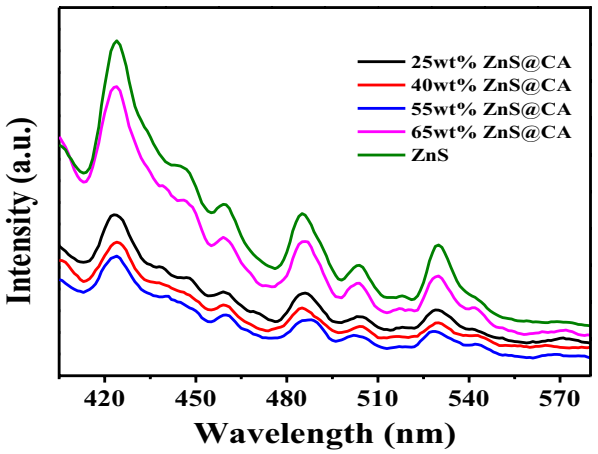

Fig. 11 PL spectra of ZnS and ZnS@CA synthesized with different ZnS content. (Color figure online)

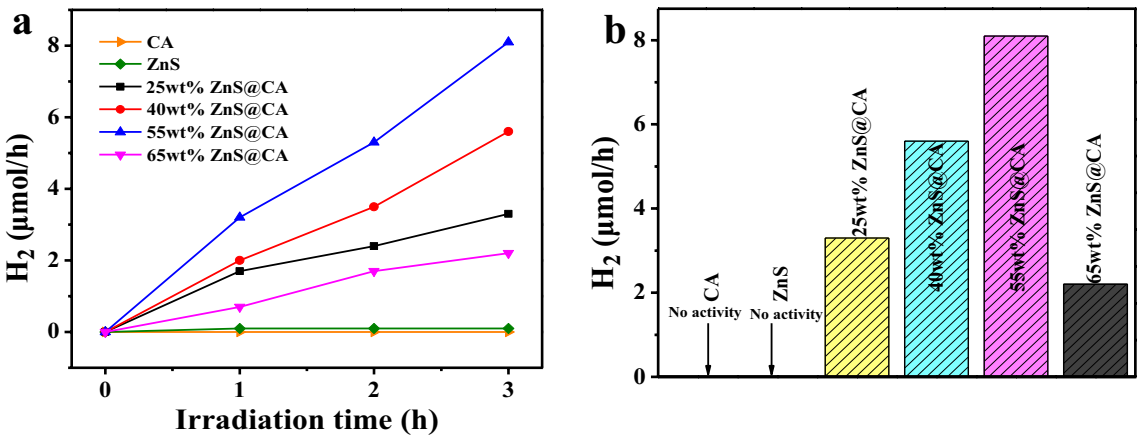

Fig. 10 Photocatalytic hydrogen evolution of CA, ZnS and ZnS@CA synthesized with different ZnS content

recombination rate of photogenerated electron–hole pairs, which is similar to the photocatalytic performances results. This result clearly showed that 55 wt%ZnS@CA materials exhibits the lowest PL emission intensity, which demonstrates that the introduction of ZnS to CA improves the separation efficiency of electron–hole pairs, resulting to enhance the photocatalytic performance. Therefore, it can be concluded that the hollow spheres of ZnS are well dispersed on the surface of CA which have the unique 3D porous network structure to formation of positive effective interfacial contacts. This is beneficial to promote charge transfer efficiency, which would lead to the excellent photocatalytic activities.

3.8.2 Detection of reactive oxygen species by ESR

To further investigate the photocatalytic mechanism in depth, the main active species generated during the photocatalysis process was probed by spin-trapping ESR technique. It should be pointed out that the characteristic quadruple peaks of DMPO−·OH species were observed in the aqueous dispersions of 55 wt%ZnS@CA under visible light irradiation and no signals were detected in the dark (Fig. 12a). As shown in Fig. 12b, when the light was turned on, four characteristic peaks of DMPO−·O_2^- adducts were observed in the methanol dispersion, revealing the formation ·O_2^- radical species during the photocatalytic process. It can be seen that the peak intensity of both hydroxyl radical and superoxide radical are very strong during the photocatalytic reaction. Therefore, according to the ESR analysis, it can be inferred that the ·OH and ·O_2^- radicals are the main active species for the photodegradation process.

Based on our experimental results, a proposed photocatalytic mechanism for the catalytic activity of the ZnS@CA mateirals is proposed in Fig. 13. When the ZnS@CA is irradiated with visible light, ZnS can be stimulated. The electrons can be excited from the VB to the corresponding CB. Due to the sufficient interface contact between CA and ZnS, the excited electron in the CB of ZnS tends to transfer to the surface of CA, leaving photogenerated holes in the VB of ZnS. Thus, high-efficiency charge separation has been achieved, corresponding wiht the result of DRS and PL analysis. The photogenerated electrons in the surface of CA are capable of reducing H^+ (O_2) into H_2 ($O_2^{\cdot -}$) for hydrogen production and MB degradation. At the same time, the holes in the VB of ZnS can convert H_2O and OH^- to ·OH, which is also the important participant in photodegradation. In addition, unique 3D porous of CA not only prevent the particulate aggregation of ZnS, but also reduce the band gap of it [26, 42, 48]. Moreover, synergistic effects between ZnS and CA may be beneficial for the improved

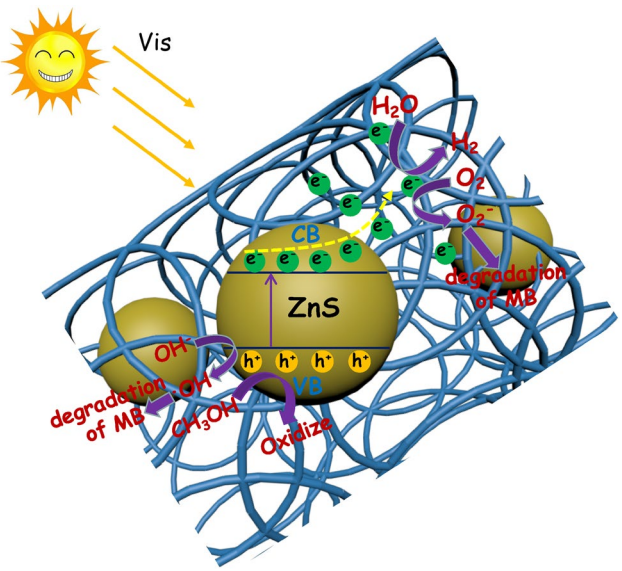

Fig. 13 Proposed mechanism for photocatalytic degradation of MB and H_2 evolution under visible light irradiation

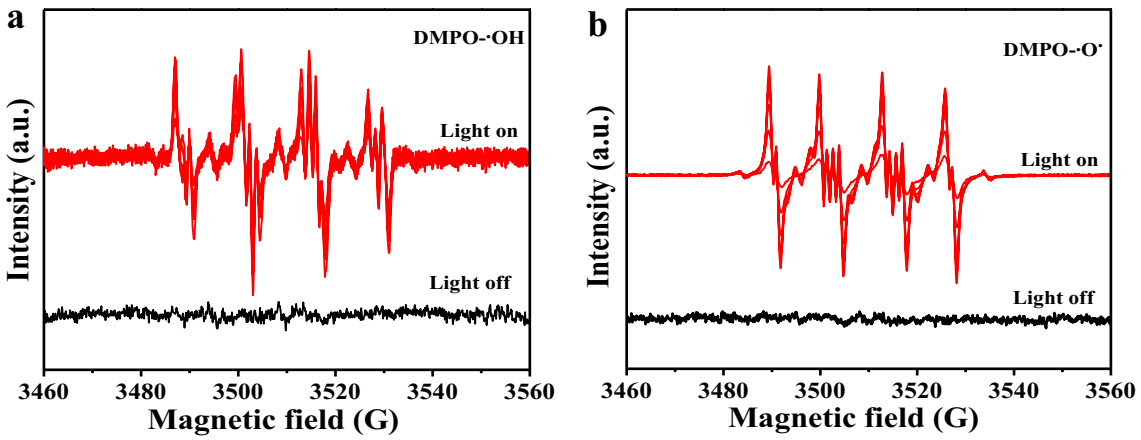

Fig. 12 DMPO spin-trapping ESR spectra for 55 wt%ZnS@CA **a** DMPO−·OH in aqueous dispersions. **b** DMPO−·O_2^- in methanol dispersions

photocatalytic performance: substantial oxygen-containing functional groups in the CA can provide abundant adsorption sites and active sites, and multiple reflections of light in the ZnS hollow spherical can increase the capture efficiency of visible light and thereby generate more photogenerated electron–hole pairs [40]. Thus, the higher photocatalytic activity can be ascribed for the high-efficiency utilization of the lights and separation of charge carriers.

4 Conclusions

In summary, the ZnS@CA photocatalysts were synthesized using waste biomass. Compared to other ZnS@CA materials, the outstanding photocatalytic performance is obtained for 55 wt%ZnS@CA by degradation of MB and photocatalytic hydrogen evaluation, and 55 wt%ZnS@CA also enhances to the fast generation, separation and transportation of photogenerated charge carriers, and avoids the photocorrosion during the photocatalytic reactions because it produces the sufficient contact interface between reactants and surface of catalyst and has the synergetic properties (as observed in SEM and HR-TEM), as the substantial oxygen-containing functional groups provide abundant adsorption sites, active sites (as observed in FT-IR spectra) and a lower recombination rate of photogenerated electron–hole pairs (as examined by PL spectra). In addition, the macroscopic block material can be easily recycled by separating from MB solution just using tweezers. The present study will open a new opportunity toward the design and practical photocatlytic applications of CA modified with other metal sulfides.

Acknowledgements The authors gratefully acknowledged the National Natural Science Foundation (21676129, 21607063, 51402130), China Postdoctoral Science Foundation (2016M590421) and the Science & Technology Foundation of Zhenjiang (GY2016021 and GY2014028), and the Science & Technology Foundation of Yangzhou Zhenjiang(GY2016021, GY2017001 and YE201709).

References

1. C.L. Yu, W.Q. Zhou, H. Liu, Y. Liu, D.D. Dionysiou, Chem. Eng. J. **287**, 117–129 (2016)
2. J. Tian, R.Y. Liu, Z. Liu, C.L. Yu, M.C. Liu, Chin. J. Catal. **38**, 1999–2008 (2017)
3. J. Tian, Z. Wu, Z. Liu, C.L. Yu, K. Yang, L.H. Zhu, W.Y. Huang, Y. Zhou, Chin. J. Catal. **38**, 1899–1908 (2017)
4. U.A. Joshi, A. Palasyuk, D. Arney, P.A. Maggard, J. Phys. Chem. Lett. **1**, 2719–2726 (2010)
5. B. Chai, T.Y. Peng, P. Zeng, X.H. Zhang, X.J. Liu, J. Phys. Chem. C **115**, 6149–6155 (2011)
6. K. Maeda, K. Domen, J. Phys. Chem. C **111**, 7851–7861 (2007)
7. Y. Yan, C. Wang, X. Yan, L.S. Xiao, J.H. He, W. Gu, W.D. Shi, J. Phys. Chem. C **118**, 23519–23526 (2014)
8. D.G. Chen, F. Huang, G.Q. Ren, D.S. Li, M. Zheng, Y.J. Wang, Z. Lin, Nanoscale **2**, 2062–2064 (2010)
9. B. Siebers, L. Biadala, D.R. Yakovlev, A.V. Rodina, T. Aubert, Z. Hens, M. Bayer, Phys. Rev. B **91**, 155304 (2015)
10. S. Thangavel, K. Krishnamoorthy, S.J. Kim, G. Venugopal, J. Alloys Compd. **683**, 456–462 (2016)
11. X.X. Yu, J.G. Yu, B. Cheng, B.B. Huang, Chem. Eur. J. **15**, 6731–6739 (2009)
12. A.P. Davis, C.P. Huang, Water Res. **25**, 1273–1278 (1991)
13. S.H. Elder, F.M. Cot, Y. Su, S.M. Heald, A.M. Tyryshkin, M.K. Bowman, Y. Gao, A.G. Joly, M.L. Balmer, A.C. Kolwaite, K.A. Magrini, D.M. Blake, J. Am. Chem. Soc. **122**, 5138–5146 (2000)
14. H. Zhang, X.J. Lv, Y.M. Li, Y. Wang, J.H. Li, ACS Nano **4**, 380–386 (2009)
15. T. Hirakawa, P.V. Kamat, J. Am. Chem. Soc. **127**, 3928–3934 (2005)
16. C.L. Yu, Y. Bai, J.C. Chen, W.Q. Zhou, H.B. He, J.C. Yu, L.H. Zhu, S.S. Xue, Sep. Purif. Technol. **154**, 115–122 (2015)
17. A.M. Turek, I.E. Wachs, E. DeCanio, J. Phys. Chem. **96**, 5000–5007 (1992)
18. B.N. Patil, S.A. Acharya, Adv. Mat. Lett. **5**, 113–116 (2014)
19. F. Gu, C.Z. Li, S.F. Wang, Inorg. Chem. **46**, 5343–5348 (2007)
20. M.H. Hsu, C.J. Chang, H.T. Weng, ACS Sustainable Chem. Eng. **4**, 1381–1391 (2016)
21. E. Unur, Microporous Mesoporous Mater. **168**, 92–101 (2013)
22. T.Y. Ying, K.L. Yang, S. Yiacoumi, C. Tsouris, J. Colloid Interface Sci. **250**, 18–27 (2002)
23. Y.Q. Li, Y.A. Samad, K. Polychronopoulou, S.M. Alhassan, K. Liao, ACS Sustainable Chem. Eng. **2**, 1492–1497 (2014)
24. Y.M. Ren, Q. Xu, J.M. Zhang, H.X. Yang, B. Wang, D.Y. Yang, J.H. Hu, Z.M. Liu, ACS Appl. Mater. Interfaces **6**, 9689–9697 (2014)
25. M. Miao, G.L. Wang, S.M. Cao, X. Feng, J.H. Fang, L.Y. Shi, Phys. Chem. Chem. Phys. **17**, 24901–24907 (2015)
26. M.J. Shi, W. Wei, Z.F. Jiang, H.K. Han, J.R. Gao, J.M. Xie, RSC Adv. **6**, 25255–25266 (2016)
27. Y.Q. Li, Y.A. Samad, K. Polychronopoulou, S.M. Alhassan, K. Liao, J. Mater. Chem. A **2**, 7759–7765 (2014)
28. F.F. Shi, L.L. Chen, C.S. Xing, D.L. Jiang, D. Li, M. Chen, RSC Adv. **4**, 62223–62229 (2014)
29. Y.J. Zhang, H.R. Xu, Q.B. Wang, Chem. Commun. **46**, 8941–8943 (2010)
30. B. Hu, S.H. Yu, K. Wang, L. Liu, X.W. Xu, Dalton Trans. **40**, 5414–5423 (2008)
31. R.J. White, V. Budarin, R. Luque, J.H. Clark, D.J. Macquarrie, Chem. Soc. Rev. **38**, 3401–3418 (2009)
32. M.K. Joshi, A.P. Tiwari, H.R. Pant, B.K. Shrestha, H.J. Kim, C.H. Park, C.S. Kim, ACS Appl. Mater. Interfaces **7**, 19672–19683 (2015)
33. B. Grzyb, C. Hildenbrand, S.B. Fabry, D. Bégin, N. Job, A. Rigacci, P. Achard, Carbon **48**, 2297–2307 (2010)
34. L. Sun, Y.J. Zhang, X.S. Ye, H.N. Liu, H.F. Zhang, A.G. Wu, Z.J. Wu, ACS Sustainable Chem. Eng. **5**, 7700–7708 (2017)
35. H.P. Cong, X.C. Ren, P. Wang, S.H. Yu, ACS Nano **3**, 2693–2703 (2012)
36. Z.Q. Wang, P.X. Jin, M. Wang, G.H. Wu, C. Dong, A.G. Wu, ACS Appl. Mater. Interfaces **8**, 32862–32868 (2016)
37. X.L. Wu, T. Wen, H.L. Guo, S.B. Yang, X.K. Wang, A.W. Xu, ACS Nano **4**, 3589–3597 (2013)
38. D.A. Reddy, R. Ma, M.Y. Choi, T.K. Kim, Appl. Surf. Sci. **324**, 725–735 (2015)
39. H. Zhao, Y.M. Dong, P.P. Jiang, G.L. Wang, H.Y. Miao, R.X. Wu, L.G. Kong, J.J. Zhang, C. Zhang, ACS Sustainable Chem. Eng. **3**, 969–977 (2015)
40. Z.F. Jiang, C.Z. Zhu, W.M. Wan, K. Qian, J.M. Xie, J. Mater. Chem. A **4**, 1806–1818 (2016)
41. D.L. Jiang, L.L. Chen, J.M. Xie, M. Chen, Dalton Trans. **43**, 4878–4885 (2014)

42. J. Di, J.X. Xia, M.X. Ji, B. Wang, S. Yin, Q. Zhang, Z.G. Chen, H.M. Li, Appl. Catal. B: Environ. **183**, 254–262 (2016)
43. Z.Y. Zhang, D.L. Jiang, D. Li, M.Q. He, M. Chen, Appl. Catal. B: Environ. **183**, 113–123 (2016)
44. Y.Y. Fan, W.G. Ma, D.X. Han, S.Y. Gan, X.D. Dong, L. Niu, Adv. Mater. **27**, 3767–3773 (2015)
45. Z.J. Sun, B.H. Lv., J.S. Li, M. Xiao, X.Y. Wang, P.W. Du, J. Mater. Chem. A **4**, 1598–1602 (2016)
46. B.Y. Chen, W.Q. Fan, B.D. Mao, H. Shen, W.D. Shi, Dalton Trans. **46**, 16050–16057 (2017)
47. C.L. Yu, F.F. Cao, X. Li, G. Li, Y. Xie, J.C. Yu, Q. Shu, Q.Z. Fan, J.C. Chen, Chem. Eng. J. **219**, 86–95 (2013)
48. D. Liu, Z.F. Jiang, C.Z. Zhu, K. Qian, Z.Y. Wu, J.M. Xie, Dalton Trans. **45**, 2505–2516 (2016)